TU Delft

Delft University of Technology

Document Version
Final published version

Licence
CC BY

Citation (APA)
Cintra, G., Koetsier, M., Mylonopoulos, V., & Pavlovic, M. (2026). Influence of fracture toughness on multi-axial loading interaction criteria for wrapped composite X-joints. *Thin-Walled Structures*, *228*, Article 115143. https://doi.org/10.1016/j.tws.2026.115143

Important note
To cite this publication, please use the final published version (if applicable).
Please check the document version above.

Copyright
In case the licence states “Dutch Copyright Act (Article 25fa)”, this publication was made available Green Open Access via the TU Delft Institutional Repository pursuant to Dutch Copyright Act (Article 25fa, the Taverne amendment). This provision does not affect copyright ownership.
Unless copyright is transferred by contract or statute, it remains with the copyright holder.

Sharing and reuse
Other than for strictly personal use, it is not permitted to download, forward or distribute the text or part of it, without the consent of the author(s) and/or copyright holder(s), unless the work is under an open content license such as Creative Commons.

Takedown policy
Please contact us and provide details if you believe this document breaches copyrights.
We will remove access to the work immediately and investigate your claim.

*This work is downloaded from Delft University of Technology.*

Thin–Walled Structures 228 (2026) 115143

Contents lists available at ScienceDirect

Thin-Walled Structures

journal homepage: www.elsevier.com/locate/tws

Full length article

# Influence of fracture toughness on multi-axial loading interaction criteria for wrapped composite X-joints

Gisele Cintra [a,c], Mathieu Koetsier [a], Vasileios Mylonopoulos [b], Marko Pavlovic [a,*]

[a] Faculty of Civil Engineering and Geoscience, Technical University Delft, Delft 2600 AA, the Netherlands
[b] Tree Composites B.V., Rotterdamseweg 266a, Delft 2628 AS, the Netherlands
[c] Department of Structures and Foundations, State University of Rio de Janeiro (UERJ), Maracanã, Rio de Janeiro 20550–013, Brazil

ARTICLE INFO

*Keywords:*
Off-shore wind
Wrapped composite joints
Multi-axial loading
Fracture toughness
Finite element modeling

ABSTRACT

Wrapped composite joints arise as an innovative solution for joining circular non-welded hollow sections (CHS) in jacket support structures for offshore wind, intending to enhance fatigue performance and consequently reduce weight and costs when compared to traditional welded joints. Due to combined waves and wind loads, these joints are subjected to different multi-axial loading scenarios. Therefore, it becomes fundamental to establish an interaction criterion that accurately predicts the failure behavior provided by the superposition of different load conditions. In this context, this paper aims to present the results of a numerical investigation on the multi-axial load behavior of wrapped composite joints. Based on previous standards for welded tubular joints [1, 2], a multi-axial loading interaction criterion is proposed for wrapped composite tubular joints, and a finite-element (FE) model is developed using the cohesive zone model approach. Eighteen loading cases, with different combinations of axial load and bending moments, were applied in a medium-scale X-shaped wrapped joint to derive the corresponding failure envelope. Three values of fracture toughness were considered to evaluate the influence of this fracture parameter on the interaction failure criteria exponents. It was concluded that the given exponents are not significantly affected by the change of interfacial strength and fracture toughness, which represents a valuable finding for the development of future design guidelines.

## 1. Introduction

The global energy transition is driving the expansion of offshore wind farms, particularly in deep waters, where most offshore wind resources are located, thereby increasing the need for innovative solutions and technological development for offshore structural foundations. The use of jackets for supporting large wind turbines is a very good alternative due to their less usage of steel when compared, for instance, to monopiles, leading to a higher cost-effectiveness. Typically, the jackets are composed of circular hollow section (CHS) joints, which are generally fabricated by welding the brace members directly to the chord members. Nevertheless, this type of foundation faces significant challenges related to the welded joints, which are prone to fatigue damage due to the high stress concentration at this location and end up governing the structure design according to their fatigue resistance. This solution leads to a less economical design due to the need to use thicker tubes to avoid fatigue failure in the welded corners [3]. A comprehensive overview of challenges associated with the complex behavior of tubular joints in marine structures is provided in [4].

In recent years, research efforts have been made to improve the performance of welded joints using fiber-polymer composites for strengthening, due to their corrosion and fatigue resistance, lightweight and potential to reduce stress concentration at nodal regions [4]. Nassiraei [5], for instance, proposed a probabilistic model to quantify the Degree of Bending (DoB) and predict the performance of tubular welded X-joints strengthened with fiber-polymer composites under axial and in-plane bending loads. Zavvar and Guedes Soares [6] investigated the effects of different fiber-polymer composite reinforcements on the stress concentration factors (SCFs) in uniplanar welded DKT-joints subjected to compressive loading. The authors found that composite reinforcement can reduce the SCF in the joint by up to 43% when compared to an unreinforced joint. In addition, it was observed that the SCF can be reduced by increasing fiber-polymer thickness and number of layers. Nassiraei et Rezadoost [7] investigated the static capacity of X-joints retrofitted with fiber-polymer composites under compressive load, proposing a formula to predict the joints ultimate strength. Their results

* Corresponding author.
*E-mail address:* M.Pavlovic@tudelft.nl (M. Pavlovic).

https://doi.org/10.1016/j.tws.2026.115143
Received 31 January 2026; Received in revised form 8 May 2026; Accepted 15 May 2026
Available online 21 May 2026
0263-8231/© 2026 The Author(s). Published by Elsevier Ltd. This is an open access article under the CC BY license (http://creativecommons.org/licenses/by/4.0/).

showed that fiber-composite strengthening can significantly improve the initial stiffness, ultimate capacity and failure mechanisms of these joints.

In a parallel context, Pavlovic *et al.* [3] proposed the concept of wrapped composite joints, which emerge as an innovative *non-welded* solution to connect circular hollow sections (CHS) in jacket support structures, intending to replace traditional welded brace-chord connections by wrapping the steel tubes with composite material fully entrusting the transfer of the joint forces to bonding. The given composite wrap is composed of glass fibers and polymeric matrix, which allows a smoother load transfer at the joints by reducing stress concentration, and therefore, enhancing fatigue endurance. Consequently, this solution enables significant weight and cost reduction when compared to conventional welded joints. Recent research has shown that wrapped composite joints can achieve fatigue lives up to 5000 times greater than those of conventional welded joints [8,9]. Previous papers have also demonstrated that, under uniaxial loading, the wrapped composite joints present higher stiffness and ultimate load-bearing resistance when compared to welded equivalents [10]. Nevertheless, in practical applications, this loading condition is unlikely to occur in isolation, since these joints are often subjected to complex multi-axial loading when connecting the brace members, due to the action of wind, wave loads and tidal forces. The coupled effects of axial forces and bending moments therefore play a critical role in joint behavior and require a thorough understanding of the joint's ultimate load capacity under combined loading scenarios. Previous research has reported experimental findings on the multi-axial behavior of these joints, pointing out the composite joints' remarkable bending resistance and rotation capacity prior to failure [11]. Moreover, previous experiments indicated that there is no significant change between failure modes when compared to uniaxial loading, showing that the joints presented a consistent onset of failure at the steel-composite interface, which progresses towards the wrapping end above the steel brace [11]. However, there is still a gap related to the interaction criteria for joints subjected to simultaneous axial and bending forces, especially when it concerns the exponents of the multi-axial loading interaction criterion.

With respect to traditional welded CHS joints, the interaction between axial force and bending has been widely investigated. Hoadley and Yura [12,13] conducted tests on double-tee tubular joints (X-joint) subjected to various combinations of loading and observed an approximately linear interaction between axial force and out-of-plane bending, particularly for a brace-to-chord diameter ratio ($\beta$) equal to 1.0. On the other hand, it was found that the interaction between axial force and in-plane bending is non-linear and approaches a quadratic relationship. Comparable behaviour was also reported by Makino et al. [14] for single T-joints subjected to combined axial loads and out-of-plane bending. In order to consider the interaction between axial and bending force in welded joints, current international standards (*e.g.* [15–17]) recommend the multi-axial interaction criterion expressed in Eq. (1), in accordance with the findings presented in Hoadley and Yura works [12,13]. In Eq. (1), $N_x$, $M_{ip}$ and $M_{op}$ denote the internal force and the in-plane and out-of-plane bending moments in the tubular joint, respectively, while $N_{x,u}$, $M_{ip,u}$ and $M_{op,u}$ represent the corresponding resistances associated with the design axial force and the in-plane and out-of-plane bending moments, respectively.

$$\frac{N_x}{N_{x,u}} + \left[\frac{M_{ip}}{M_{ip,u}}\right]^2 + \frac{|M_{op}|}{M_{op,u}} \leq 1,0 \tag{1}$$

In this context, it is important to remind that, in wrapped composite joints, the load is transferred mainly through bonding between steel and composite instead of welding. Therefore, further investigation is needed to determine the accurate exponents of the multi-axial interaction criterion to be applied in composite joints design. Aiming to accomplish this objective, it is also fundamental, at an earlier stage, to understand the sensitivity of these exponents to fracture parameters and determine whether it plays an important role in the multi-axial interaction. This necessity is further amplified by the challenges associated with determining fracture toughness, which often requires the conduction of extensive experimental programs involving specialized set-ups. This difficulty is compounded by the lack of specific standards for different composites and bi-materials, combined with the scarcity of fracture mechanics data in the literature, which hinders the validation with numerical models. Moreover, depending on the quality control and production method, these composites materials may exhibit high variability in mechanical properties, which can affect the fracture parameters. Therefore, assessing the sensitivity of the multi-axial interaction exponents to fracture toughness can substantially reduce the time and resources required for future research and projects, while also contributing to the development of design guidelines and more reliable failure prediction.

Given these considerations, this paper aims to investigate the influence of fracture toughness on the multi-axial loading criterion for wrapped composite joints, while also providing starting-point values for the exponents to be adopted in interaction equations in future design codes for steel tubular members wrapped with composites. A numerical parametric study is conducted based on the cohesive zone model (CZM) approach to predict the failure of the wrapped composite joint. Three different fracture toughness values were assessed, and eighteen loading cases were evaluated for each fracture toughness, comprising uniaxial, biaxial and full multi-axial loading conditions. In all, fifty-four models were analyzed to estimate failure envelopes and to provide a comprehensive understanding of the problem, including variations in ultimate loads and bending moments. Finally, the influence of the fracture parameters on the multi-axial interaction criterion exponents is evaluated and discussed.

## 2. Joint material and geometry

This paper addresses the behavior of an X-joint [11], which is used to connect brace members in offshore structures. To facilitate comparison with existing and future laboratory experiments, the investigated structure is a medium scale joint, representing approximately 1/4 of a typical full-scale joint. It is composed of four steel CHS tubes (two chords and two braces positioned perpendicular to each other) made of grade S355 steel, with an outer diameter of 168 mm and a wall thickness of 12.5 mm, as shown in Fig. 1. The steel tubes are wrapped by a multi-directional composite, with glass woven fabric and chopped strand mat (CSM) embedded in a thermosetting vinyl ester resin, which is manufactured through a hand-lamination procedure. The respective orientations of the glass fibers in the joint are illustrated in Fig. 1. The composite wrap is directly laminated over the steel tubes, and no adhesive layer is placed between the two materials [18]. A nominal composite thickness of 16 mm at the joint root is considered, with a wrapping length equal to 252 mm on the braces (see Fig. 1). The top and bottom flanges shown in Fig. 1 are usually attached to the composite joints as components of experimental test fixtures. To enable future comparisons, these flanges are also included in the numerical model presented in this investigation.

## 3. Numerical investigation

### 3.1. Material properties

The X-joint is simulated numerically in a 3D stress finite element (FE) model using Abaqus/Explicit 2023 v.6.26 [19] to optimize convergence issues. The elastic material properties of steel and composite wrap were calibrated based on previous experiments on the material [20,21] and are listed in Table 1. The anisotropic yielding behavior of the composite wrap component is taken into account based on preliminary experiments while, for steel tubes, plasticity is disregarded to prevent steel from yielding before complete interface debonding or failure in the

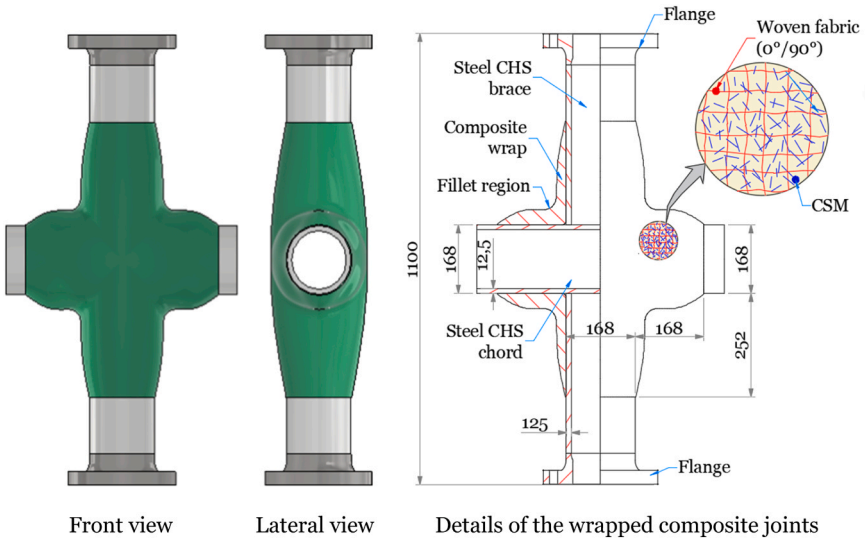



**Fig. 1.** Overview and detail of the studied 90° X-joint.

**Table 1**
Material properties of steel and composite wrap.

| | Mechanical Property | Average value (MPa) |
|---|---|---|
| *Steel* | Elastic modulus ($E_s$) | 210,000 |
| | Poisson's coefficient | $\nu = 0.3$ |
| *Composite wrap* | Longitudinal and transverse modulus ($E_{x,c}$=$E_{y,c}$) | 11,800 |
| | Transverse modulus ($E_{z,t}$) | 5721 |
| | In-plane shear modulus ($G_{xy}$) | 2550 |
| | Out-of-plane shear modulus ($G_{xz}$ =$G_{yz}$) | 1819 |
| | Poisson's coefficient | $\nu_{xy}$= 0.22; $\nu_{xz}$= $\nu_{yz}$= 0.35 |

composite material. To evaluate the influence of disregarding plastic behavior for steel, preliminary numerical analyses incorporating both plastic and elastic material models were assessed. It was observed that for the loading case involving axial load only, no significant differences were observed in terms of ultimate loads or overall load-displacement response. On the other hand, for the loading cases in which bending moments are dominant over axial loads, the joints were allowed to reach higher ultimate bending moments when disregarding steel plasticity. This observation is relevant because, although the joints are expected to experience steel yielding prior to interfacial debonding and/or composite wrap failure, previous experiments showed that, when upscaling from medium scale to full-scale joints, the ultimate debonding resistance increases with a lower factor than the steel resistance. Therefore, building a numerical campaign that allows ultimate bending moments to exceed those limited by steel plasticity is important to contribute to future design procedures and gather knowledge related to failure associated with interfacial debonding and composite material. For this reason, the failure envelope generated in this paper concerns only the composite wrap.

### 3.2. Mesh elements and size

As shown in Fig. 2a, four-node linear tetrahedrons (C3D4) were used in a free mesh to model the composite wrap due to its capacity to simulate complex and curved geometries. This type of element was also chosen for well-capturing out-of-plane shear displacements, which are inherent to the debonding process at the steel-composite interface. On the other hand, eight-node linear hexahedral elements (C3D8R) were used in a semi structured mesh to model the steel chords and braces due

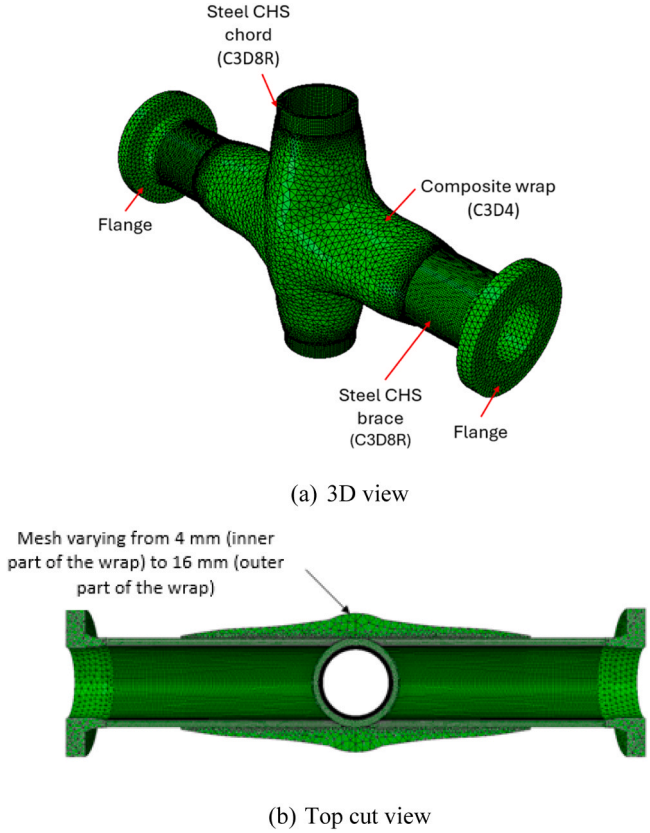



**Fig. 2.** Mesh configuration for wrapped composite X-joints: (a) 3D view; (b) Top cut view.

to their higher accuracy and stability in nonlinear/dynamic analyses, besides offering more computational efficiency to simulate simpler geometries. As previously mentioned, the flanges were included in the numerical model for future comparisons and were discretized using four-node linear tetrahedrons (C3D4) elements in a mesh size of 12 mm. A mesh sensitivity analysis was carried out considering different mesh sizes for the steel components and for both the inner and outer parts of composite wrap. Based on this convergence mesh study, a global mesh size of 4 mm was adopted for the CHS steel components, whereas, for the

composite wrap, sizes varying from 4 mm (close to the end of the wrap) up to 16 mm (towards the X-joint center) were adopted, as shown in Fig. 2a. A size mesh transition with a growth factor of 4 was also introduced between the outer and inner parts of the composite wrap, as presented in Fig. 2b. Smaller-sized elements were adopted in the inner region of the composite, close to the interface, since the mesh sensitivity analyses indicated that load transfer is more influenced by the composite mesh elements near the bonded surface.

### 3.3. Cohesive zone model

In order to simulate the damage on the composite-steel interface, cohesive zone model (CZM) approach was used. The initial cohesive stiffness $K_0$ was considered as 100.000 N/m$^3$, following references from previous data reported in the literature [22,23]. Cohesive behavior was introduced in the model as a general contact interaction property and applied to the interface composite-steel. Four-linear shape traction separation laws, presented in Fig. 3, were defined based on previous experiments [24,25], in order to describe the fracture behavior for pure mode I and pure mode II. In order to introduce different proportions of mode mixity, three intermediate cohesive laws, representing 25%, 50% and 75% of Mode II were established through the interpolation of values obtained for pure mode I and pure mode II.

In Fig. 3, the points "p", "c", "b" and "f" indicate four critical stages identified in previous double-cantilever beams (DCB) and end-notched flexure (ENF) experiments conducted on this material [24,25]. These points represent, respectively, the onset of plastic deformation (p), the onset of cracking (c), the onset of fiber bridging mechanism (b) and the specimen failure (f). The subscripts "I" and "II" in Fig. 3 refer to pure Mode I and pure Mode II, respectively. The mentioned stages are mainly due to three different mechanisms corresponding to different areas below the σ-δ curve: *1) crack tip deformation*: described by the area between points "p" and "c", which is associated to crack initiation or crack tip fracture resistance ($G_{tip}$); *2) softening mechanism,* represented by the area between points "c" and "b" and associated to the weak resistance of the resin, which is pulled out from the micro valleys of the steel surface; and *3) fiber bridging mechanism*, defined by the area between points "b" and "f" and related to the strain energy release rate (SERR) dissipated due to fiber bridging. It is worth pointing out that, for Mode I, the influence on SERR dissipation due to softening is considered negligible and could be considered as part of $G_{tip,}$ in agreement with the literature [26,27]. On the other hand, the softening mechanism is found to contribute significantly to the Mode II fracture resistance of wrapped composite joint interface [22] (see plateau for pure Mode II in Fig. 3) and therefore, it is treated as a distinct fracture process. More information concerning the definition of the cohesive laws can be found in [24,25].

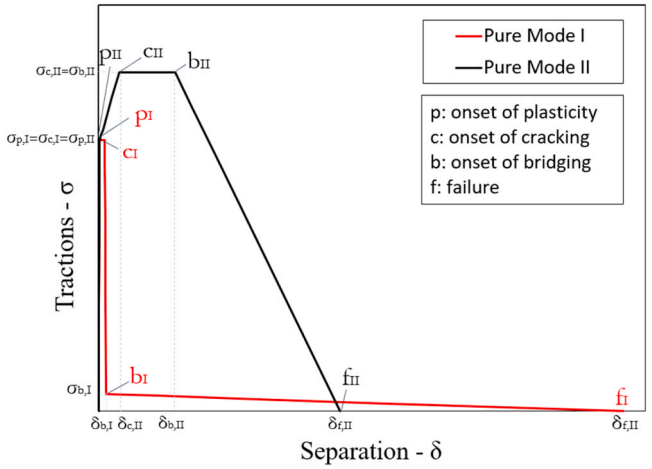



**Fig. 3.** Traction separation laws for pure Modes I and II.

### 3.4. Assessed fracture toughness

In order to investigate the influence of the fracture toughness ($G_c$) on the multi-axial behavior of wrapped composite X-joints, three values of $G_c$ were selected based on previous experiments conducted on medium-scale steel-composite coupons [21]: $G_{c,1}$ = 7.5 N/mm; $G_{c,2}$ = 6 N/mm and $G_{c,3}$ = 4.5 N/mm. Fig. 4 illustrates the rate of traction reduction used to vary the values of fracture toughness for both Mode I and Mode II. Using the fracture toughness $G_{c,1}$ = 7.5 N/mm as a reference value, the cohesive laws corresponding to $G_{c,2}$ = 6 N/mm and $G_{c,3}$ = 4.5 N/mm were obtained by mainly reducing the interfacial strength in 20% and 40%, respectively. As a result, the strain energy release rates (SERR) associated with crack-tip deformation, softening mechanism and fiber bridging were proportionally scaled for both Mode I, II and intermediate mode-mixity ratios.

### 3.5. Load application and boundary conditions

The axial force ($N_x$) and out-of-plane ($M_{op}$) and in-plane ($M_{ip}$) bending moments were applied symmetrically at the reference points RP−1 and RP−2, as shown in Fig. 5. The force was axially applied in the X direction, while the out-of-plane and in-plane bending moments were applied around the Y and Z axes, respectively. A first attempt at using the common deformation control approach was conducted. However, an apparent spurious compression in the steel chord in the X direction was noticed in cases where the bending moment is dominant, leading to a high non-linearity in the results. Therefore, to avoid this issue, load control was chosen to be used in this work. To simulate the boundary conditions and provide stability to the X-joint, two internal nodes at the joint center were restrained in the Y direction, while four nodes (at the bottom and the top of the chord) were restrained in the X and Y directions, as illustrated in Fig. 5.

### 3.6. Assessed loading cases

With the aim of derive a three-dimensional failure envelope for wrapped composite joints from numerical results (see Fig. 6), different proportions of axial loads and bending moments were applied, resulting in a total of eighteen load combinations for each assessed fracture toughness. This number was selected based on a convergence study, in which additional loading combinations were evaluated, leading to a

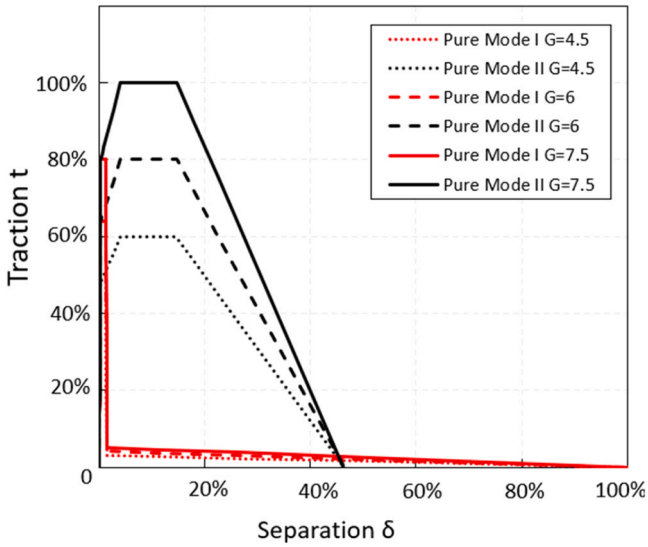



**Fig. 4.** Proportion of traction reduction in the variation of fracture toughness.

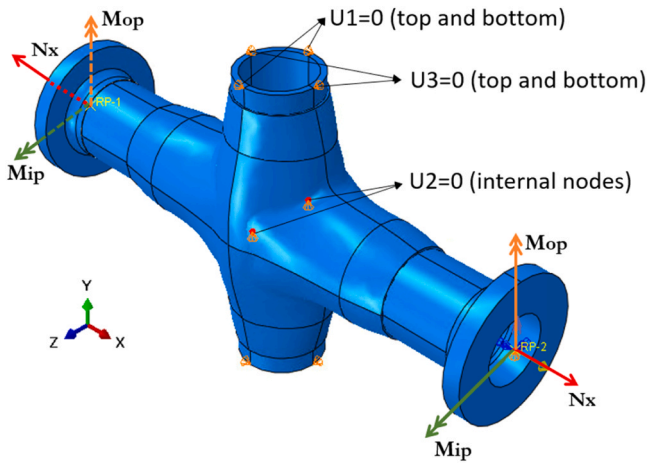
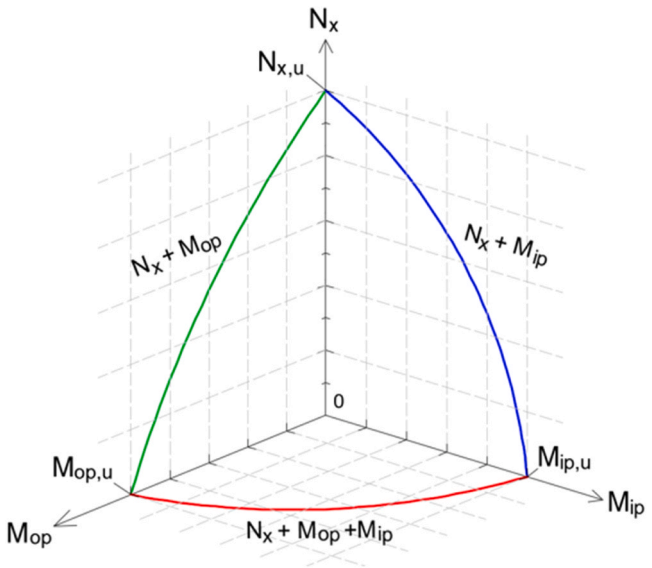



**Fig. 5.** Load/Moment application and boundary conditions.




*Multi-axial interaction criterion:*

$$\left(\frac{Nx}{Nx_u}\right)^{\alpha} + \left(\left[\frac{Mop}{Mop_u}\right]^{\beta} + \left[\frac{Mip}{Mip_u}\right]^{\gamma}\right)^{\zeta} = 1$$

**Fig. 6.** Typical 3D failure envelope to be derived from numerical results.

total of twelve cases per 2D plane – equivalent to thirty-six loading cases for a three-dimensional envelope. No significant changes were observed in the shape, boundaries, or exponent values of the resulting ultimate load envelope, indicating that a set of eighteen loading cases for each fracture toughness value provides a sufficiently accurate representation.

As previously mentioned, three values of fracture toughness were evaluated in this parametric study to understand the influence of this fracture parameter in the multi-axial interaction criterion: $G_{c,1} = 7.5$ N/mm; $G_{c,2} = 6$ N/mm and $G_{c,3} = 4.5$ N/mm, resulting in a total of fifty-four models. Table 2 summarizes the eighteen loading cases (LC) evaluated for each of the three fracture toughness values considered in this work. The given loading combinations are also illustrated in Fig. 7 to facilitate comprehension. In Table 2, the load combinations are basically grouped into three categories, which corresponds to the three planes illustrated in Fig. 6: *a)* Plane $N_x + M_{op}$; *b)* Plane $N_x + M_{ip}$; *c)* Plane $N_x + M_{op} + M_{ip}$. Planes *a)* and *b)* include mainly *biaxial loading cases* involving the combination of axial force and bending moments in a single direction (LC2-LC5 and LC8-LC11), also comprising *uniaxial cases* with pure axial force $N_x$ (LC1 and LC7) and only bending moments $M_{op}$ or $M_{ip}$ (LC6 and L12). The plane *c)* predominantly encompasses the *full-multi-axial loading cases*, with combination of axial force and simultaneous bending moments in two directions (LC14-LC17). This plane also includes a *uniaxial case* with pure axial force (LC13) and a *biaxial loading case* combining in-plane and out-of-plane bending moments (LC18).

The column entitled "Load combinations" in Table 2 specifies the different proportions of axial loads and bending moments applied in the numerical model in order to facilitate reader comprehension. The maximum values of axial force and bending moments considered in the FE model were 1700 kN and 200 kN.m, respectively, which corresponds to uniaxial cases that were defined as having 100% of the applied load. Accordingly, in loading case 2 (LC2), for instance, the proportion $0.88\ N_x + 0.40\ M_{op}$ indicates that 88% of the maximum force and 40% of the maximum out-of-plane bending moments were applied, corresponding to values of 1500 kN and 80 kN.m, respectively. Furthermore, the magnitudes of the bending moments applied simultaneously in two directions were calculated to maintain the same proportional relationship as those applied in the loading cases with single direction bending moments.

It is worth pointing out that the development of this numerical model was supported by extensive laboratory experiments previously reported in literature [10,24,25,28–31]. Additionally, the numerical results presented in the following sections were validated against experimental data for the loading cases involving axial load only (LC1 =LC7 =LC13), out-of-plane bending only (LC6) and in-plane bending only (LC12). The complete experimental program, including detailed descriptions of used test setups, will be presented in future work.

## 4. Results and discussion

### 4.1. Load vs. displacement curves

Fig. 8 presents the load *vs.* displacement curves corresponding to all assessed loading cases for the fracture toughness $G_{c,1} = 7.5$. The black curve corresponds to the uniaxial loading case with axial force only, while the blue and red curves represent the biaxial loading combinations $N_x + M_{op}$ and $N_x + M_{ip}$, respectively. In addition, the full multi-axial cases ($N_x + M_{ip} + M_{op}$) are presented by the green curves.

The five black rectangular markers indicated on the LC1 ($N_x$) curve correspond to the different loading stages illustrated in Fig. 9, which presents the debonding progression by the red region visible in the front-view cut of the composite wrap. The interface debonding is tracked in the numerical model using the Cohesive Surface Damage Variable (CSDM), which varies from 0 (undamaged) to 1 (fully damaged/debonded). It can be noticed that the X-joints exhibit non-linear behavior prior to failure for all loading conditions. The loss of linearity occurs when debonding at the interface steel-composite initiates at the joint root. As the applied loading increases, debonding at the steel-composite interface progresses predominantly towards the end of the braces, with some extension into the chord as well, as shown in Fig. 9. This trend was consistently observed for all evaluated loading cases.

The ultimate capacity was determined based on the peak load – or, for cases involving pure bending, the maximum moment – which, for all loading cases, coincided with the maximum deformation prior to failure. For combined axial and bending loading cases, the corresponding pair of axial loads and bending moments at the peak load was considered. As expected, the loading cases LC1 =LC7 =LC13 (Nx), with only axial forces applied in the model, resulted in the highest ultimate load value, equal to 1576 kN. On the other hand, for both biaxial (Nx+Mip and Nx+Mop) and full multi-axial loading cases (Nx+Mip+Mop), it can be observed that the ultimate load tends to decrease with increasing proportions of bending moments. For instance, the loading cases LC5 (0.12 Nx + Mop), LC11 (0.12 Nx + Mip), and LC17 (0.12 Nx + 0.71Mip + 0.71Mop), with dominance of bending moments over axial forces,

**Table 2**
Assessed multi-axial loading cases.

| | *Loading case (LC)* | *Load combinations* | *Applied $N_x$ (kN)* | *Applied $M_{op}$ (kN.m)* | *Applied $M_{ip}$ (kN.m)* |
|---|---|---|---|---|---|
| *Nx+Mop plane* | LC1 | $N_x$ | 1,700 | 0 | 0 |
| | LC2 | 0.88 $N_x$ + 0.40 $M_{op}$ | 1,500 | 80 | 0 |
| | LC3 | 0.53 $N_x$ + 0.60 $M_{op}$ | 900 | 120 | 0 |
| | LC4 | 0.29 $N_x$ + 0.75 $M_{op}$ | 500 | 150 | 0 |
| | LC5 | 0.12 $N_x$ + $M_{op}$ | 200 | 200 | 0 |
| | LC6 | $M_{op}$ | 0 | 200 | 0 |
| *Nx+Mip plane* | LC7=LC1 | $N_x$ | 1,700 | 0 | 0 |
| | LC8 | 0.88 $N_x$ + 0.40 $M_{ip}$ | 1,500 | 0 | 80 |
| | LC9 | 0.53 $N_x$ + 0.60 $M_{ip}$ | 900 | 0 | 120 |
| | LC10 | 0.29 $N_x$ + 0.75 $M_{ip}$ | 500 | 0 | 150 |
| | LC11 | 0.12 $N_x$ + $M_{ip}$ | 200 | 0 | 200 |
| | LC12 | $M_{ip}$ | 0 | 0 | 200 |
| *Nx+Mop+Mip plane* | LC13=LC7=LC1 | $N_x$ | 1,700 | 0 | 0 |
| | LC14 | 0.88 $N_x$ + 0.28 $M_{op}$ + 0.28 $M_{ip}$ | 1,500 | 57 | 57 |
| | LC15 | 0.53 $N_x$ + 0.42 $M_{op}$ + 0.42 $M_{ip}$ | 900 | 85 | 85 |
| | LC16 | 0.29 $N_x$ + 0.53 $M_{op}$ + 0.53 $M_{ip}$ | 500 | 106 | 106 |
| | LC17 | 0.12 $N_x$ +0.71 $M_{op}$ +0.71 $M_{ip}$ | 200 | 141 | 141 |
| | LC18 | 0.71 $M_{op}$ + 0.71 $M_{ip}$ | 0 | 200 | 200 |

presented the lowest ultimate axial loads, with values between 133 kN and 165 kN. In contrast, the biaxial loading cases LC2 (0.88 Nx + 0.40 Mop), LC8 (0.88 Nx + 0.40 Mip), and LC14 (0.88 Nx + 0.28 Mip + 0.28 Mop), characterized by a high dominance of axial forces relative to bending moments, presented ultimate load values ranging from 1220 kN and 1264 kN, *i.e.*, 77% to 80% of the highest ultimate load achieved among all loading cases.

### 4.2. Moment vs. rotation curves

Figs. 10 and 11 present the moments *vs.* rotation curves associated with out-of-plane and in-plane moments, respectively, for the fracture toughness $G_{c,1} = 7.5$. As expected, the loading cases with only bending moments applied LC6 ($M_{op}$) and LC12 ($M_{ip}$) presented the highest bending resistances, with ultimate out-of-plane and in-plane moments equal to 161.5 kN.m and 140 kN.m, respectively. As can be seen, in general, the out-of-plane bending resistance is slightly higher than the in-plane resistance, not only due to the greater out-of-plane composite thickness at the X-joint root, but also due to less local bending of the laminate in the corners (see fillet region in Fig. 1).

Analogously to the load *vs.* displacement curves response, the ultimate bending resistances increase as bending moments become more dominant relative to the axial forces. For instance, the previously mentioned biaxial loading cases LC5 (0.12 $N_x$ + $M_{op}$) and LC11 (0.12 $N_x$ + $M_{ip}$) presented the second-highest ultimate bending moments, with values equal to 145.4 kN.m and 128.5 kN.m, respectively. On the other hand, the combination of axial force and bending moments in two different directions in loading case LC17 (0.12 $N_x$ + 0.71 $M_{ip}$ + 0.71 $M_{op}$) led to ultimate bending moments approximately 37% lower than those of the biaxial cases with same proportion of applied loading (LC5 and LC11).

### 4.3. Influence of fracture toughness on response curves

Fig. 12 presents a comparison of load *vs.* displacement curves obtained for the three values of fracture toughness evaluated in this work

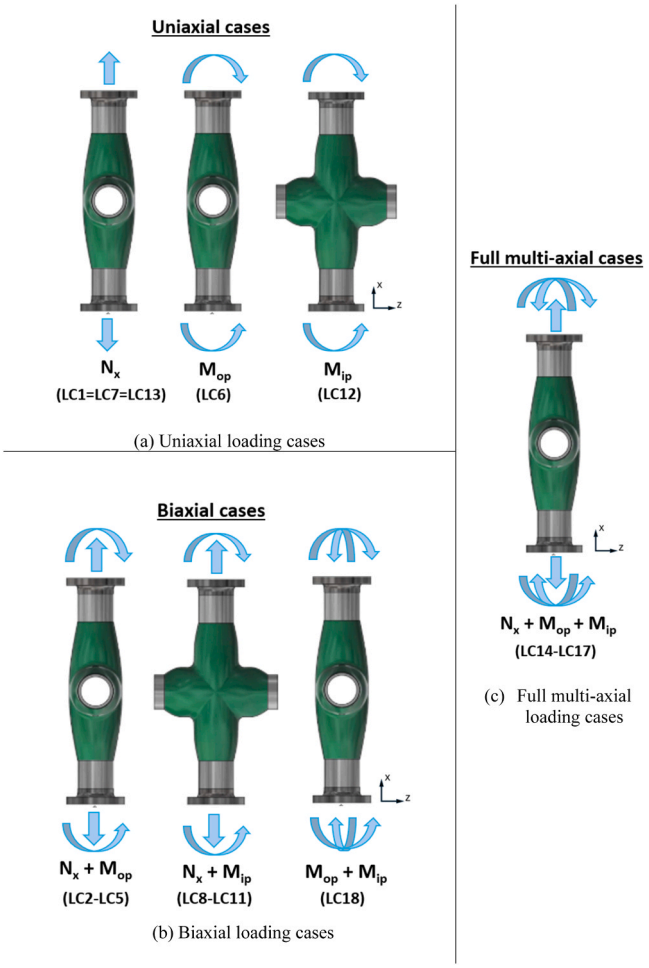



**Fig. 7.** Scheme of the assessed loading cases.

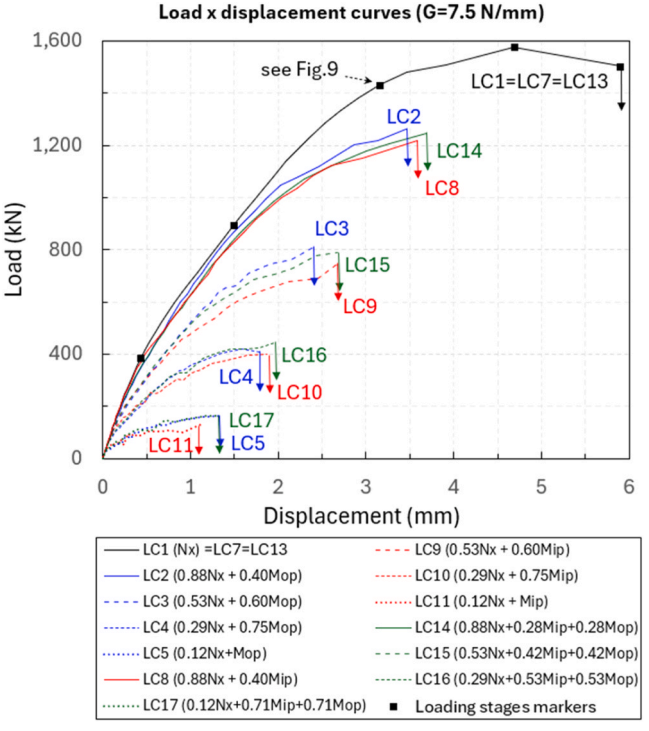



**Fig. 8.** Load *vs.* displacement curves for $G_{c,1} = 7.5$ N/mm.

($G_{c,1}$ =7.5 N/mm; $G_{c,2}$ =6 N/mm and $G_{c,3}$ =4.5 N/mm). For clarity and ease of comparison, only the uniaxial loading case LC1 and the full multi-axial cases LC14-LC17 are presented. These results are considered representative, as identical trends were observed for biaxial loading cases. Figs. 13 and 14 present the corresponding results in terms of moment *vs.* rotation curves. For completeness, the summary of joint resistances for different fracture toughness values is presented in section 4.8.

From Figs. 12–14, it can be noticed that a higher fracture toughness value leads to a slight improvement in ductile behavior. Moreover, as expected, reductions in fracture toughness resulted in decreases in both ultimate axial loads and bending moments, with a greater influence observed on the former. Considering all evaluated loading cases, a 20% reduction in the steel–composite interfacial strength for both Modes I and II led to an average decrease of approximately 12% in the ultimate axial load. In the same scenario, average reductions of 10% and 9% were found for ultimate out-of-plane and in-plane bending moments, respectively. Similarly, when reducing the fracture toughness in 40%, average reductions of around 23%, 21% and 20% were observed for the resistant axial force and ultimate out-of-plane and in-plane bending moments, respectively.

In general, variations in the fracture toughness led to more pronounced differences in the ultimate axial forces for loading cases dominated by bending moments (*e.g.* LC17 - 0.12 $N_x$ + 0.71 $M_{op}$ + 0.71 $M_{ip}$). For instance, as shown in Fig. 12, in loading case LC14 (0.88 $N_x$ + 0.28 $M_{op}$ + 0.28 $M_{ip}$), ultimate loads of 1246 kN and 1100 kN were obtained for fracture toughness values of 7.5 N/mm and 6 N/mm, respectively, thereby resulting in a decrease of approximately 11.7%. On the other hand, for the loading case LC17 (0.12 $N_x$ + 0.71 $M_{op}$ + 0.71 $M_{ip}$), the same analysis led to a difference of 16%.

With respect to variations in ultimate bending moments, a reduction in fracture toughness led to comparable decreases, with slightly larger reductions in out-of-plane than in-plane bending moments for most loading cases. As shown in Figs. 13 and 14, for the loading case LC17 (0.12 $N_x$ + 0.71 $M_{op}$ + 0.71 $M_{ip}$), the ultimate out-of-plane bending moment presented a decrease of 13% after a reduction of 20% in the interfacial strength, compared to a 10% decrease in the ultimate in-plane bending moment. Similarly, for the loading case LC16 (0.29 $N_x$ + 0.53 $M_{op}$ + 0.53 $M_{ip}$), the same reduction in the fracture toughness resulted in decreases of 9% and 7.5% in ultimate out-of-plane and in-plane bending moments, respectively. For a reduction of 40% in fracture toughness, the differences between ultimate in-plane and out-of-plane moments became even smaller for loading cases dominated by bending moments. In the previously mentioned loading case LC17 (0.12 $N_x$ + 0.71 $M_{op}$ + 0.71 $M_{ip}$), the reductions in ultimate out-of-plane and in-plane bending moments in this case were, respectively, 25% and 24%.

### 4.4. Deformed shape

Fig. 15a illustrates the typical joint deformation shape for a full multi-axial loading case (LC15 – 0.53 $N_x$ + 0.42 $M_{op}$ + 0.42 $M_{ip}$), corresponding to an applied load of P = 590.4 kN and a fracture toughness of 6 N/mm. The debonded length between the steel tubes and the composite wrap was tracked using the previously defined variable CSDM and the deformation was amplified by a factor of 15 to facilitate the visualization.

The deformation at failure is shown in Fig. 15b through a 3D cut view, in which is possible to observe the detachment between the steel and the composite wrap, resulting in complete debonding at the braces. Similar deformation trends were found for all loading cases, with damage initiating at the joint center at the level of chords and braces and progressing toward the wrapping end above the steel braces, as previously shown in Fig. 9. However, as expected, both the type of loading combination and the proportion of applied bending moments influence the symmetry of the debonding progression, depending on which side of

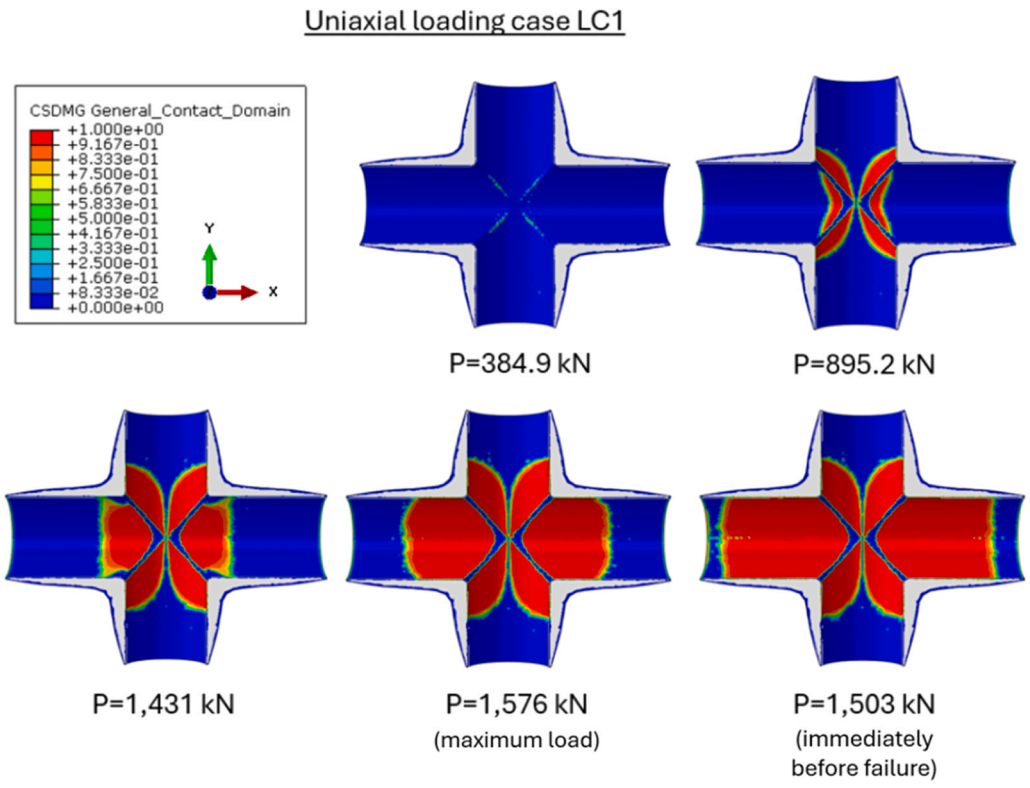



**Fig. 9.** Front-view cut of the composite wrap: debonding at different loading stages.

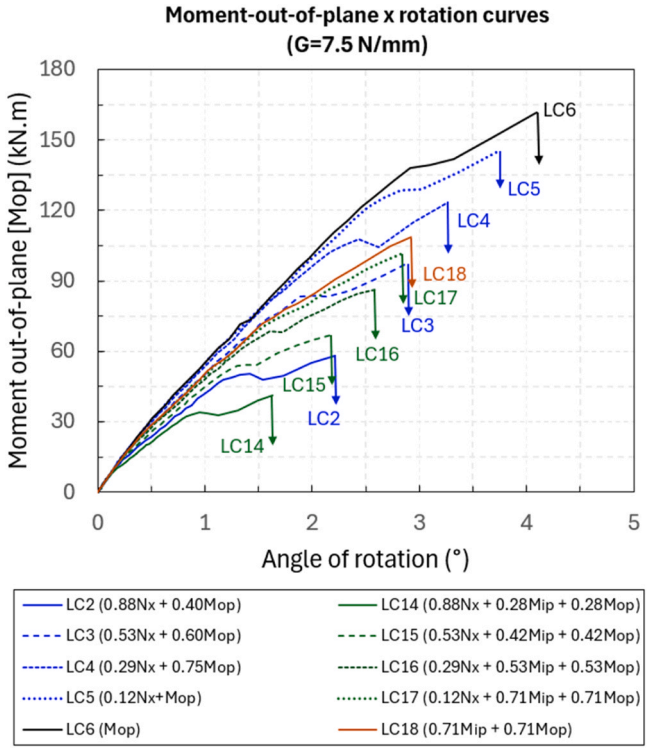



**Fig. 10.** Out-of-plane bending moment *vs.* angle of rotation curves for $G_{c,1}$ = 7.5 N/mm.

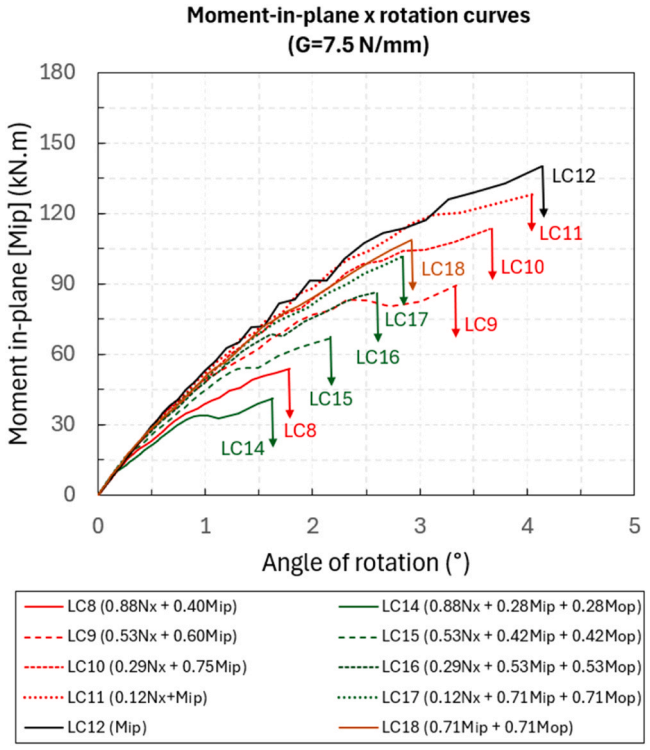



**Fig. 11.** In-plane bending moment *vs.* angle of rotation curves for $G_{c,1}$ = 7.5 N/mm.

the joint is subjected to higher stresses.

### 4.5. *Multi-axial interaction criterion for wrapped composite joints*

Preliminary analyses were conducted for the proposition of a multi-axial interaction criterion of wrapped composite joints and have shown

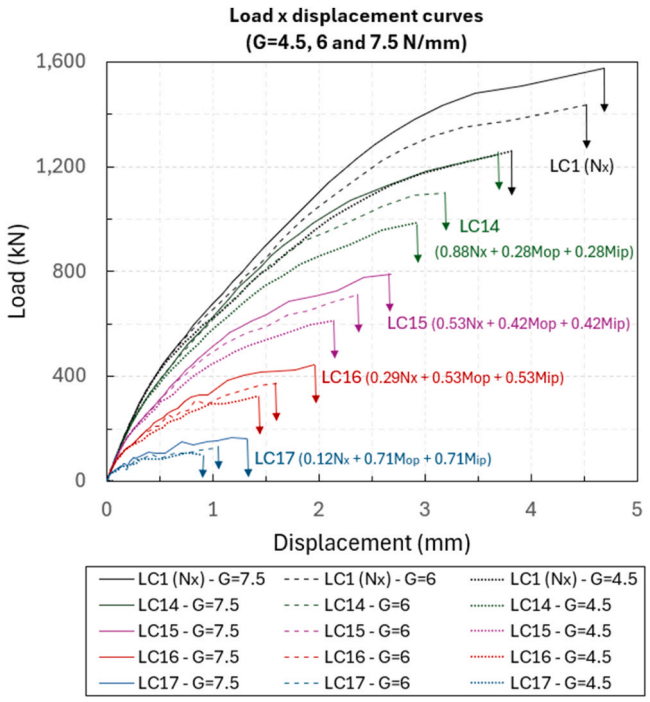



**Fig. 12.** Load *vs.* displacement curves of uniaxial case LC1 and full multi-axial cases LC14-LC17 for all values of fracture toughness evaluated.

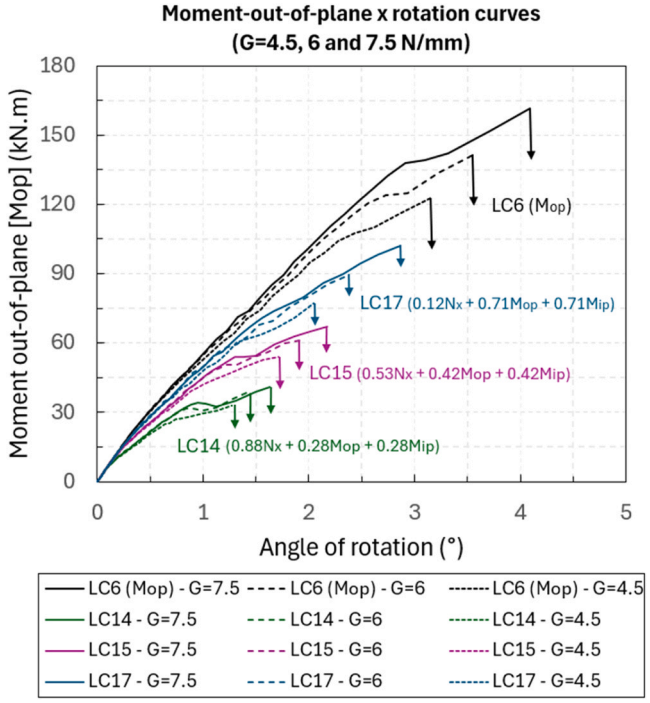



**Fig. 13.** Moment out-of-plane *vs.* rotation curves of uniaxial case LC6 and full multi-axial cases LC14-LC17 for all values of fracture toughness evaluated.

that, in cases where axial loads act simultaneously with bending forces, the joint resistance is underestimated when considering a linear summation of the normalized strength values. Therefore, further studies are needed to determine the optimum interaction criterion exponents. Based on previously mentioned existing standards [1,2] addressing the multi-axial loading interaction criterion for offshore structures, Eq. (2) can be proposed to design the wrapped composite joint subjected to

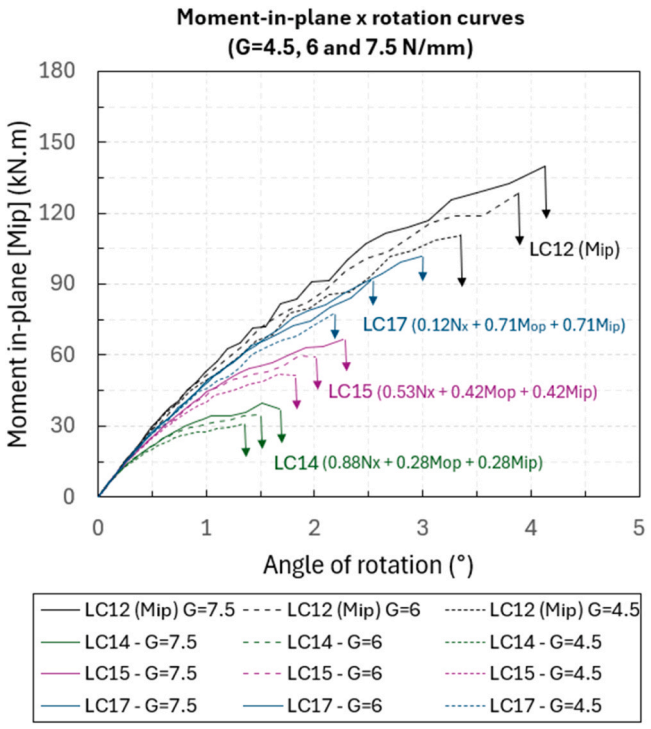



**Fig. 14.** Moment in-plane *vs.* rotation curves of uniaxial case LC12 and full multi-axial cases LC14-LC17 for all values of fracture toughness evaluated.

combined axial tension and out-of-plane bending forces.

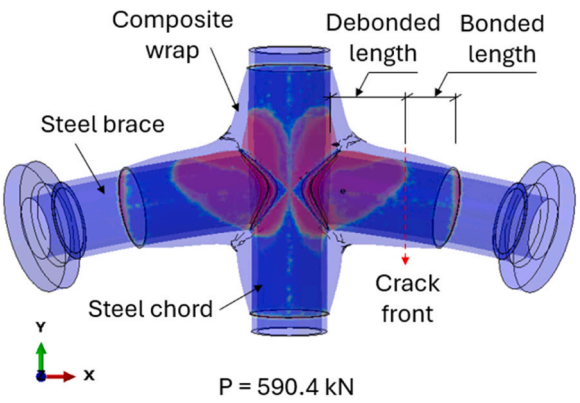
$$\left(\frac{N_x}{N_{x,u}}\right)^{\alpha} + \left(\left[\frac{M_{op}}{M_{op,u}}\right]^{\beta} + \left[\frac{M_{ip}}{M_{ip,u}}\right]^{\gamma}\right)^{\zeta} = 1 \tag{2}$$

Where $N_x$, $M_{op}$ and $M_{ip}$ are the design values for the tensile axial force, moment out-of-plane and moment in-plane, respectively, whereas $N_{x,u}$, $M_{op,u}$ and $M_{ip,u}$ are the corresponding ultimate values associated with loading cases LC1 =LC7 =LC13 ($N_x$), LC6 ($M_{op}$) and LC12 ($M_{ip}$), respectively. The parameters $\alpha$, $\beta$, $\gamma$ and $\zeta$ are the proposed interaction exponents to be calibrated based on the numerical results presented in the following sections. Specifically, the parameters $\alpha$, $\beta$ and $\gamma$ correspond to the exponents of the normalized axial force, out-of-plane bending moment, and in-plane bending moment, respectively, while $\zeta$ governs the interaction between the bending moments.

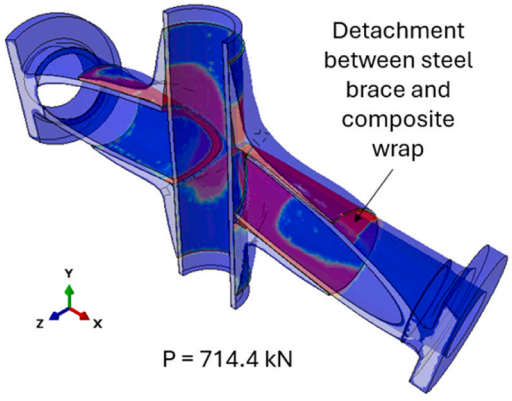
#### 4.5.1. *Interaction exponents calibration and 2D failure envelopes*

To obtain the interaction exponents $\alpha$, $\beta$, $\gamma$ and $\zeta$, a curve was fitted to the numerical data by a non-linear regression through the least square method for each fracture toughness value. Table 3 presents the multi-axial interaction exponents that provide the best fit to the numerical curves. The numerical results used for the calibration of the given exponents are presented in Fig. 16 for each plane defining the three-dimensional failure envelope illustrated in Fig. 6. In other words, Fig. 16a, b and c present 2D failure envelopes for the $N_x + M_{op}$, $N_x + M_{ip}$ and $N_x + M_{ip} + M_{op}$ planes, respectively. The results are expressed in terms of ultimate axial forces $N_x$ plotted against the ratio $\sqrt{M_{ip}{}^2 + M_{op}{}^2}$, where $M_{ip}$ and $M_{op}$ are the ultimate in-plane and out-of-plane bending moments for each loading case. The purple, blue and green markers represent the numerical outcomes for all loading combinations considering the three fracture toughness values evaluated in this work. In parallel, the solid lines represent the fitted curves used to determine the exponents α, β, γ and ζ, and are shown together with the associated coefficient of determination ($R^2$).

It can be seen that the two-dimensional failure envelopes for $G_{c,1}$,




(a) Front view showing debonding progress




(b) 3D cut view showing deformation at failure.

**Fig. 15.** Deformed shape of the joint for the LC15 (0.53 $N_x$ + 0.42 $M_{op}$ + 0.42 $M_{ip}$) and $G_{c,2}$ = 6 N/mm: (a) Front view showing debonding progression; (b) 3D cut view showing deformation at failure.

**Table 3**
Interaction exponents found for the fracture toughness $G_{c,1}$ = 7.5 N/mm, $G_{c,2}$ = 6 N/mm and $G_{c,3}$ = 4.5 N/mm.

| G = 7.5 N/mm | G = 6 N/mm | G = 4.5 N/mm |
|---|---|---|
| α = 0.89 | α = 0.87 | α = 0.88 |
| β = 2.27 | β = 2.30 | β = 2.32 |
| γ = 2.11 | γ = 2.11 | γ = 2.14 |
| ζ = 0.70 | ζ = 0.71 | ζ = 0.71 |

$G_{c,2}$, and $G_{c,3}$ presented consistent results between each other. The fitted curves agreed very well with the numerical data obtained, with greater deviations observed for the loading cases combining axial force and in-plane bending moments ($R^2$=0.995 for $G_{c,1}$ =7.5 N/mm). In general, it was observed that the relationship between the ultimate axial force and the ultimate vectorial combination of bending moments approaches a quadratic polynomial function in all three planes ($N_x$ +$M_{op}$, $N_x$ +$M_{ip}$ and $N_x$ +$M_{ip}$+$M_{op}$).

It can be also observed, through Table 3, that the exponents $\alpha$, $\beta$, $\gamma$ and $\zeta$ exhibited slight variations when decreasing the fracture toughness in 20% and 40%. The parameters $\gamma$ and $\zeta$ presented the smallest changes, with deviations of up to 1.4%, whereas $\alpha$ and $\beta$ presented differences up to 2.3%, thus indicating that these exponents are not significantly affected by variations in interfacial strength and fracture toughness.

*4.5.2. Interaction exponents calibration for $\alpha = 1.00$*

Nevertheless, in order to address practical design considerations, it might be convenient to adopt an exponent α equal to 1.0. Therefore, based on the previous calibrated exponents reported in Table 3, the exponent α was fixed as 1.0 and the remaining parameters were manually fitted to the numerical data, aiming for a minimum $R^2$ in such fitting scenario. Fig. 17 presents the resulting 2D failure envelopes for α = 1.0. Identical exponents were adopted for all fracture toughness values, and the parameters providing the best fit under the assumption $\alpha = 1.00$ were approximately $\beta = 2.25$; $\gamma = 2.03$ and $\zeta = 0.65$. In summary, the interaction exponents that best fit the numerical data shown in Fig. 17 lead to the multi-axial interaction criteria expressed by Eq. (3), where $N_x$, $M_{ip}$ and $M_{op}$ represents the design axial force and the in-plane and out-of-plane bending moments in the X-joint, respectively, while $N_{x,u}$, $M_{ip,u}$ and $M_{op,u}$ correspond to the associated ultimate values, respectively.

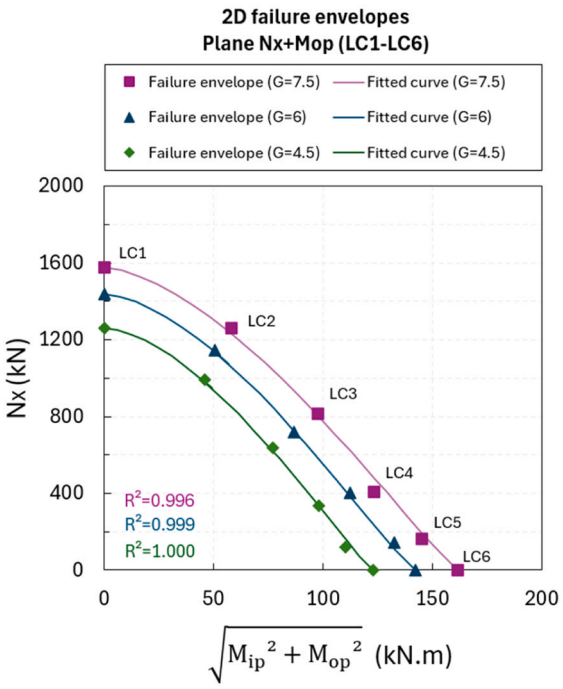
$$\left(\frac{Nx}{Nx_u}\right)^{1.0} + \left(\left[\frac{Mop}{Mop_u}\right]^{2.3} + \left[\frac{Mip}{Mip_u}\right]^{2.0}\right)^{0.7} = 1 \quad (3)$$

It can be noticed that satisfactory agreement was also achieved by fixing the parameter $\alpha$ as 1.0. As can be seen in Fig. 17b, slightly greater deviations are observed for $G_{c,2}$ = 6 N/mm in loading cases involving combined axial tension and in-plane bending moments, with a small reduction in the coefficient of determination $R^2$ from 0.998 to 0.996. In general, although minor increase of deviations was observed when compared to the previously derived exponents, the minimum coefficient $R^2$ remained at 0.992 (see Fig. 17a), still indicating a very good agreement. For full-multi axial loading cases (see Fig. 17c), a minimum coefficient $R^2$ of 0.996 was found by fixing the parameter $\alpha$ as 1.0. Moreover, the relationship between the ultimate axial force and vectorial combination of in-plane and out-of-plane moments continues to be well approximated by a quadratic polynomial function in all three planes.

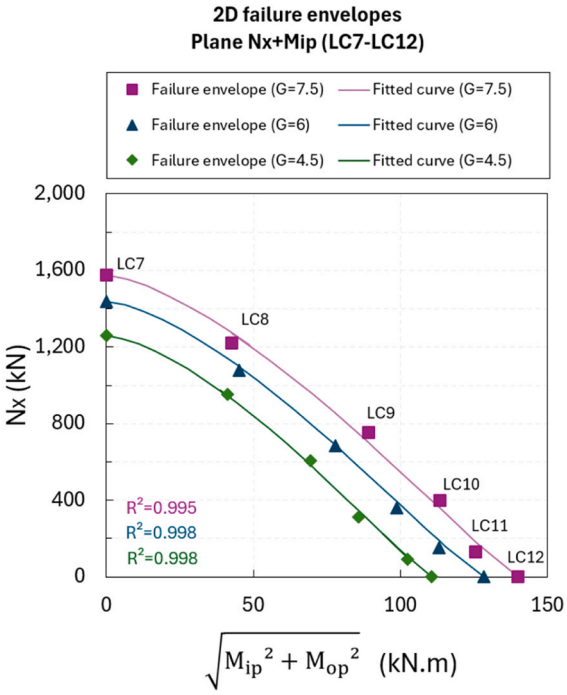
Furthermore, curves regarding different fracture toughness could be well fitted using the same multi-axial interaction exponents, thereby reinforcing that the multi-axial interaction exponents are not significantly influenced by fracture toughness values. Therefore, Eq. (3) can initially be proposed for the design of wrapped composite joints subjected to combined loading conditions, including axial loads ($N_x$), out-of-plane bending ($M_{op}$) and in-plane bending moments ($M_{ip}$). The results can be applied, for instance, by independently determining the joint resistance under axial load and bending moments, either experimentally or numerically, for different geometries and subsequently applying the interaction exponents to verify the joint under multi-axial loading conditions. This approach is consistent with current design practices for welded joints [1,2,15,16,32], in which similar interaction formulations are adopted.

Moreover, the presented results are transferable to other glass-fiber composites with different volume fractions and fiber architectures, provided they exhibit quasi-isotropic behavior. For instance, composites with higher volume fractions and consequently, higher elastic moduli, are expected to exhibit different fracture toughness thus different debonding resistance. However, as demonstrated throughout this paper, this would not affect the multi-axial interaction exponents, which are not dependent on the fracture toughness.

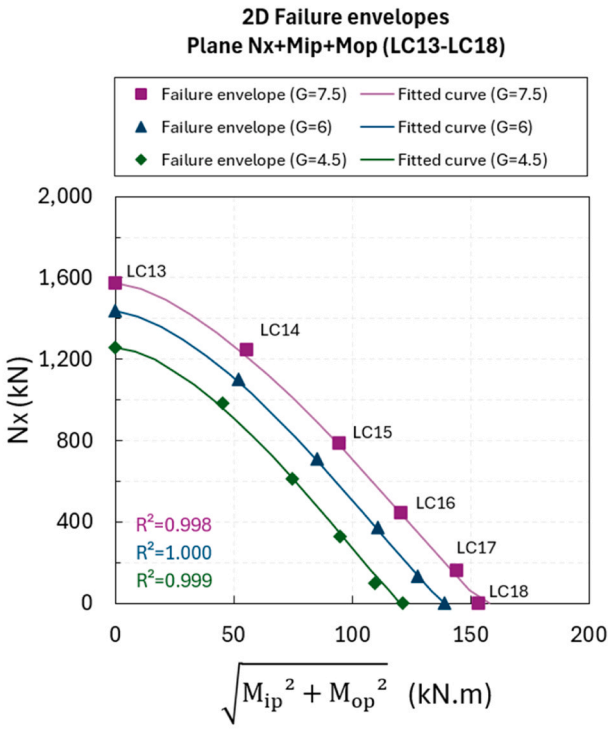
Further validation against multi-axial experimental data is planned for future work to establish the most appropriate set of exponents for wrapped composite joints. The primary objective of this paper is to demonstrate that variability in the interface fracture toughness does not significantly influence the exponents defined in Eq. (3). This understanding may contribute to a substantial reduction in time and resources waste, representing a valuable outcome for the development of future design guidelines. This is particularly relevant when considering the challenges associated with obtaining reliable fracture toughness parameters with a basis on fracture mechanics experiments, as well as the high variability typically observed in composites material properties.




(a) 2D numerical failure envelopes (plane $N_x$+$M_{op}$)




(b) 2D numerical failure envelopes (plane $N_x$+$M_{ip}$)

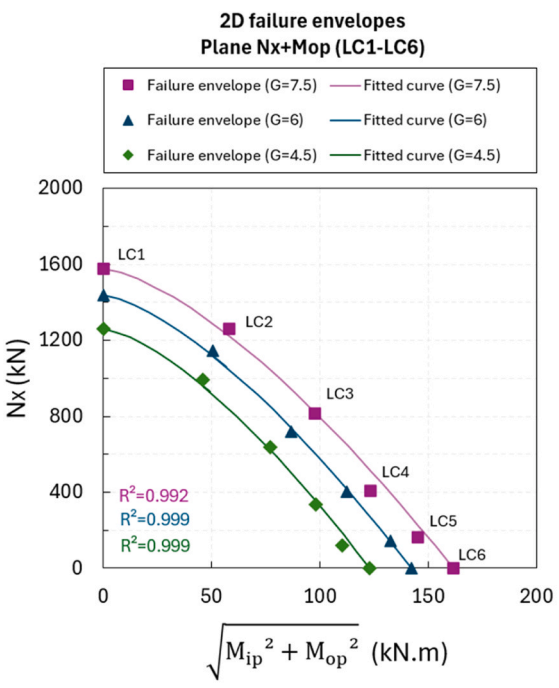



(c) 2D numerical failure envelopes (plane $N_x + M_{ip} + M_{op}$).

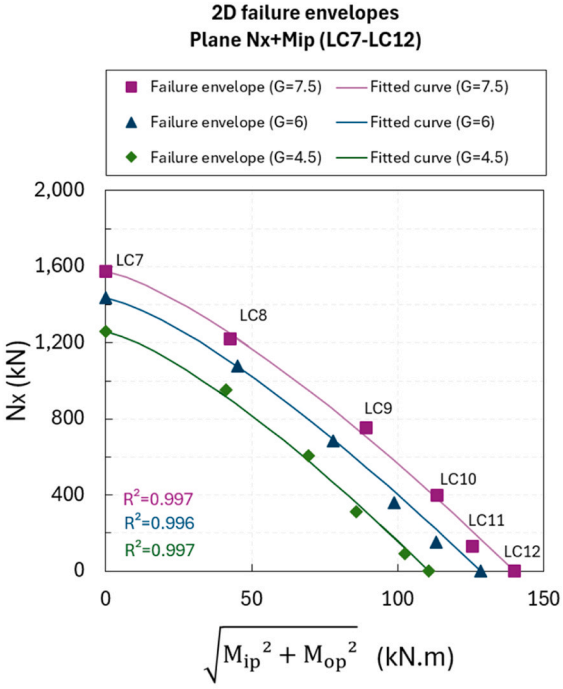
**Fig. 16.** 2D numerical failure envelopes for $G_{c,1} = 7.5$ N/mm, $G_{c,2} = 6$ N/mm and $G_{c,3} = 4.5$: (a) plane $N_x + M_{op}$; (b) plane $N_x + M_{ip}$; (c) plane $N_x + M_{ip} + M_{op}$.

## 5. Conclusions

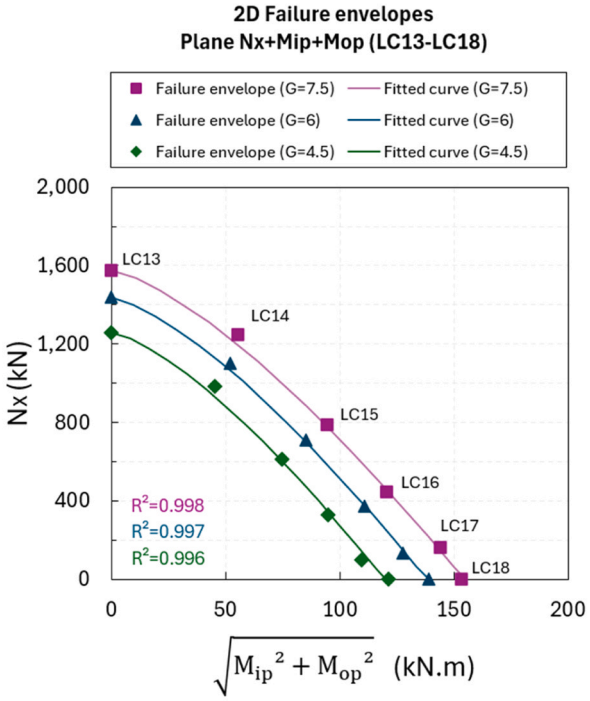
A medium-scale X-shaped wrapped composite joint was simulated using a 3D finite element model based on the CZM approach in order to assess the influence of the fracture toughness on the exponents of the multi-axial loading interaction criterion combining tensile axial force with in-plane and out-of-plane bending load in the joint. Eighteen loading cases were considered to generate the failure envelopes corresponding to three different values of fracture toughness ($G_{c,1}$ =7.5 N/mm, $G_{c,2}$ =6 N/mm and $G_{c,3}$ =4.5 N/mm). Following conclusions can be




(a) 2D numerical failure envelopes (plane $N_x$+$M_{op}$) for α=1.0




(b) 2D numerical failure envelopes (plane $N_x$+$M_{ip}$) for α=1.0.




(c) 2D numerical failure envelopes (plane $N_x + M_{ip} + M_{op}$) for α=1.0.

**Fig. 17.** 2D numerical failure envelopes for α = 1.0: (a) plane $N_x + M_{op}$; (b) plane $N_x + M_{ip}$; (c) plane $N_x + M_{ip} + M_{op}$;.

drawn from this work:

- For all loading cases, the joint experiences a steady progressive debonding between steel and composite materials at the level of chord and braces, until ultimate load.

- Reductions of fracture toughness by 20% and 40% led to proportionally less reduction of joint resistance to axial and bending loads and the combinations thereof investigated here. Reduction of fracture toughness by 20% (from 7.5 N/mm to 6.0 N/mm) led to approximately 12% and 10% decrease of resistance to axial force and bending moments, respectively. Similarly, reduction of fracture toughness by another 20% (from 6.0 N/mm to 4.5 N/mm) led to additional reduction of approximately 10% in resistance to axial force and bending moments.
- The multi-axial interaction exponents calibrated from the numerical data presented minor variation for different fracture toughness values, with differences lower than 2.3%, even when decreasing the fracture toughness up to 40%. Therefore, it can be concluded that these parameters are not significantly influenced by changes in the interfacial strength or fracture toughness.

From an engineering perspective, these conclusions imply that variations in interface quality, manufacturing methods or other factors affecting the given fracture parameter do not significantly affect the governing design check in terms of interaction exponents values. Furthermore, this finding may represent an important contribution for future design guidelines and offer a valuable simplification in the calculation procedure, especially when considering the inherent variability of composite materials and the experimental challenges associated with accurately determining fracture toughness.

## CRediT authorship contribution statement

**Gisele Cintra:** Writing – original draft, Visualization, Validation, Software, Methodology, Investigation, Formal analysis, Data curation, Conceptualization. **Vasileios Mylonopoulos:** Writing – review & editing. **Mathieu Koetsier:** Writing – review & editing, Software, Investigation. **Marko Pavlovic:** Writing – review & editing, Supervision, Software, Project administration, Methodology, Funding acquisition, Conceptualization.

## Declaration of Competing Interest

The authors declare that they have no known competing financial interests or personal relationships that could have appeared to influence the work reported in this paper.

## Acknowledgments

The authors would like to thank the Rijksdienst voor Ondernemend Nederland (RVO) for the financial support with Topsector Energiesubsidie van het Ministerie van Economische Zaken through WrapnNode-I (HER+−01085007) and WrapNode-II (HER+22–02−03442019) projects.

## Data availability

Data will be made available on request.

## References

[1] ISO 19902, Petroleum and natural gas industries, Fixed Steel Offshore Struct. 2020 (2020).
[2] Norwegian Technology Standards Institution, "NORSOK N-004:2013 - Design of Steel Structures," Norway, 2013. [Online]. Available: ⟨http://www.nts.no/norsok⟩.
[3] M. Pavlovic, M. Veljkovic, M. Segeren, Wrapped Composite Joints for Circular Hollow Section Structures, ce/Pap. 6 (3–4) (Sep. 2023) 1179–1184, https://doi.org/10.1002/cepa.2754.
[4] E. Zavvar, P. Rosa-Santos, E. Ghafoori, F. Taveira-Pinto, Analysis of tubular joints in marine structures: A comprehensive review, Jan. 01, Elsevier Ltd,, 2025, https://doi.org/10.1016/j.marstruc.2024.103702.
[5] H. Nassiraei, Probabilistic modeling of degree of bending in FRP-strengthened offshore tubular X-joints, Sci. Rep. 15 (1) (Dec. 2025), https://doi.org/10.1038/s41598-025-23024-9.
[6] E, G.S.C. Zavvar, Effects of fibre reinforced polymer on stress concentration factors in uniplanar DKT-joints subjected to the compression loading, in: C. Guedes Soares, T.A. Santos (Eds.), Trends in Maritime Technology and Engineering, Taylor & Francis, London, UK, 2022, pp. 249–257.
[7] H. Nassiraei, P. Rezadoost, Static capacity of tubular X-joints reinforced with fiber reinforced polymer subjected to compressive load, Eng. Struct. 236 (Jun. 2021), https://doi.org/10.1016/j.engstruct.2021.112041.
[8] W. Feng, M. Pavlovic, Fatigue behaviour of non-welded wrapped composite joints for steel hollow sections in axial load experiments, Eng. Struct. 249 (Dec. 2021), https://doi.org/10.1016/j.engstruct.2021.113369.
[9] M. Koetsier, V. Mylonopoulos, M. Wolters, and M. Pavlovic, "Comparative Analysis of Non-Welded Wrapped Composite Joints Versus Welded Joints Under Multi-Axial Load Conditions in Offshore Wind Turbine Supporting Structures: A Fatigue Performance Evaluation," in *ASME 2024 43rd International Conference on Ocean, Offshore and Arctic Engineering*, Singapore, 2024. doi: 10.1115/OMAE2024–124828.
[10] P. He, M. Pavlovic, Failure modes of bonded wrapped composite joints for steel circular hollow sections in ultimate load experiments, Eng. Struct. 254 (Mar. 2022), https://doi.org/10.1016/j.engstruct.2021.113799.
[11] M. Koetsier, J. Yang, and M. Pavlovic, "Experimental investigation of wrapped composite X-joints under monotonic uniaxial and multi-axial load conditions."
[12] P.W. Hoadley, Ultimate strength of tubular joints subjected to combined loads, University of Texas at Austin,, 1984.
[13] P.W. Hoadley, J.A. Yura, Ultimate Strength of Tubular Joints Subjected to Combined Loads, Offshore Technol. Conf. OTC (May 1985), https://doi.org/10.4043/4854-MS.
[14] Y. Makino, Y. Kurobane, S. Takizawa, N. Yamamoto, Behavior Of Tubular T- and K-Joints Under Combined Loads, Offshore Technol. Conf. OTC (May 1986), https://doi.org/10.4043/5133-MS.
[15] J. Wardenier, Y. Kurobane, G. Packer, G.J. v d Vegte, X.-L. Zhao, Design Guide for Circular Hollow Section (CHS) Joints Under Predominantly Static Loadin, CIDECT,, Geneva, Switzerland, 2008.
[16] D.N. Veritas, DNVGL-ST-0126: Support structures for wind turbines," Høvik, Norway, 2021.
[17] "EN 1993–1-8: Eurocode 3: Design of steel structures - Part 1–8: Design of joints."
[18] W. Feng, M. Pavlovic, M. Koetsier, M. Veljkovic, Interfacial fatigue debonding retardation in wrapped composite joints: Experimental and numerical study, Compos. Struct. 319 (Sep. 2023), https://doi.org/10.1016/j.compstruct.2023.117146.
[19] M. Smith, "ABAQUS/Standard User's Manual," 2009, *Dassault Systèmes Simulia Corp.*: Version 6.9.
[20] W. Feng, M.M. Arouche, M. Pavlovic, Fatigue crack growth characterization of composite-to-steel bonded interface using ENF and 4ENF tests, Compos. Struct. 334 (Apr. 2024), https://doi.org/10.1016/j.compstruct.2024.117963.
[21] J. Yang, M.M. Arouche, S. Egilsson, M. Koetsier, T. Peeters, M. Pavlovic, Size Effects on Mode I and Mode II Fracture Behavior of FRP–Steel Bonded Interface: Experimental and Numerical Investigation, J. Compos. Constr. 29 (2) (Apr. 2025), https://doi.org/10.1061/JCCOF2.CCENG-4760.
[22] G.G. Cintra, J.D. Vieira, D.C.T. Cardoso, T. Keller, Mode I and Mode II fracture behavior in pultruded glass fiber-polymer – Experimental and numerical investigation, Compos. B Eng. 266 (Nov. 2023), https://doi.org/10.1016/j.compositesb.2023.110988.
[23] S. Ahmadvashaghbash, M. Engül, F.E. Öz, R. Amali, and N. Ersoy, "A comparative numerical study aiming to reduce computation cost for Mode-I delamination simulations," 2018.
[24] P. He, M. Moreira Arouche, M. Koetsier, M. Pavlovic, Mode I fracture behavior of glass fiber composite-steel bonded interface – Experiments and CZM, Compos. Struct. 330 (Feb. 2024), https://doi.org/10.1016/j.compstruct.2023.117814.
[25] P. He, M. Koetsier, V. Mylonopoulos, M. Pavlovic, Mode II fracture behavior of glass fiber composite-steel bonded interface–experiments and CZM, Eng. Fract. Mech. 310 (Nov. 2024) 110510, https://doi.org/10.1016/j.engfracmech.2024.110510.
[26] A. Cameselle-Molares, A.P. Vassilopoulos, J. Renart, A. Turon, T. Keller, Numerical simulation of two-dimensional in-plane crack propagation in FRP laminates, Compos. Struct. 200 (Sep. 2018) 396–407, https://doi.org/10.1016/j.compstruct.2018.05.136.
[27] M. Heidari-Rarani, M.M. Shokrieh, P.P. Camanho, Finite element modeling of mode i delamination growth in laminated DCB specimens with R-curve effects, Compos. B Eng. 45 (1) (Feb. 2013) 897–903, https://doi.org/10.1016/j.compositesb.2012.09.051.
[28] W. Feng, P. He, M. Pavlovic, Combined DIC and FEA method for analysing debonding crack propagation in fatigue experiments on wrapped composite joints, Compos. Struct. 297 (Oct. 2022), https://doi.org/10.1016/j.compstruct.2022.115977.
[29] M.M. Arouche, M. Pavlovic, Experimental and numerical analysis of the effect of temperature on the mode I and mode II delamination of glass fiber woven composites, Compos. B Eng. 293 (Mar. 2025), https://doi.org/10.1016/j.compositesb.2025.112131.

[30] P. He, W. Feng, M. Pavlovic, Influence of steel yielding and resin toughness on debonding of wrapped composite joints, Compos. Struct. 312 (May 2023), https://doi.org/10.1016/j.compstruct.2023.116862.
[31] M. Pavlovic, P. He, M. Koetsier, and V. Mylonopoulos, "Engineering Structures Mode II fracture behavior of glass fiber composite-steel bonded interface-experiments and CZM Mode II fracture behavior of glass fiber composite-steel bonded interface 1-experiments and CZM."
[32] American Petroleum Institute (API), *API Recommended Practice 2A-WSD: Planning, Designing, and Constructing Fixed Offshore Platforms—Working Stress Design*, 22th Edition. 2014.